Materials Research Bulletin 49 (2014) 310–318

Contents lists available at ScienceDirect

Materials Research Bulletin

journal homepage: www.elsevier.com/locate/matresbu

g-C_3N_4/$NaTaO_3$ organic–inorganic hybrid nanocomposite: High-performance and recyclable visible light driven photocatalyst

Santosh Kumar [a], Bharat Kumar [b], T. Surendar [a], Vishnu Shanker [a,*]

[a] Department of Chemistry, National Institute of Technology Warangal, 506004 A.P., India
[b] Department of Chemistry, Indian Institute of Technology Delhi, New Delhi 110016, India

ARTICLE INFO

Article history:
Received 13 March 2013
Received in revised form 31 August 2013
Accepted 3 September 2013
Available online 12 September 2013

Keywords:
A. Composites
A. Nanostructures
A. Semiconductors
B. Chemical synthesis
D. Catalytic properties

ABSTRACT

Novel g-C_3N_4/$NaTaO_3$ hybrid nanocomposites have been prepared by a facile ultrasonic dispersion method. Our results clearly show the formation of interface between $NaTaO_3$ and g-C_3N_4 and further loading of g-C_3N_4 did not affect the crystal structure and morphology of $NaTaO_3$. The g-C_3N_4/$NaTaO_3$ nanocomposites exhibited enhanced photocatalytic performance for the degradation of Rhodamine B under UV–visible and visible light irradiation compared to pure $NaTaO_3$ and Degussa P25. Interestingly, the visible light photocatalytic activity is generated due to the loading of g-C_3N_4. A mechanism is proposed to discuss the enhanced photocatalytic activity based on trapping experiments of photoinduced radicals and holes. Under visible light irradiation, electron excited from the valance band (VB) to conduction band (CB) of g-C_3N_4 could directly inject into the CB of $NaTaO_3$, making g-C_3N_4/$NaTaO_3$ visible light driven photocatalyst. Since the as-prepared hybrid nanocomposites possess high reusability therefore it can be promising photocatalyst for environmental applications.

1. Introduction

Transition metal oxides with perovskite structure (such as titanium, tantalum-based semiconductor materials) have been attracted considerable attention in recent decades due to their interesting properties and potential applications [1]. Recently, $NaTaO_3$ has been found to be a highly active photocatalyst for water splitting and environmental remediation under UV light irradiation due to its physical, chemical and structural properties [2–4]. Moreover, $NaTaO_3$ has favourable band edge potentials and delocalized nature of photoexcited electrons which are primary reasons for higher efficiency [5–7]. The photocatalytic activity of $NaTaO_3$ is further enhanced by doping of alkaline earth metal ions and certain lanthanides [8,9]. In a significant development, Kato et al. showed that a maximum quantum efficiency of 56% at 270 nm irradiation can be obtained by La-doped $NaTaO_3$ loaded with NiO particles [10]. However, their activities are limited to ultraviolet (UV) region, and the component of UV in the solar spectrum is only about 4%. In order to utilize the solar energy with high conversion efficiency, absorption of wavelengths greater than 420 nm is essential. To date, studies on visible light active $NaTaO_3$ is limited. Nitrogen-doped $NaTaO_3$ catalyst has been studied for visible light driven photocatalytic degradation of methylene blue as well as gaseous formaldehyde [11,12]. A solid solution photocatalyst ($Na_{1-x}La_xTa_{1-x}Co_xO_3$ for $x = 0.0$ to $x = 0.25$) has been developed to tune the band gap towards visible region that showed hydrogen evolution from aqueous methanol solution [13]. These studies suggest that absorption can be achieved by modification of the band structure via substitutional doping of appropriate cations at 'Ta' site in $NaTaO_3$ lattice. Recently, bismuth-doped $NaTaO_3$ nanoparticles prepared by hydrothermal method have been studied for photocatalytic hydrogen evolution under visible light irradiation without adding any co-catalyst [14].

Making composite with another semiconductor material is one of the most successful ways to alter the band structure of host material and induce absorption [15–19]. In semiconductor composite materials, the recombination of photoinduced electrons and holes can be suppressed, because they can act as electron trap and promote interfacial charge transfer processes in the composite systems, thus improving photocatalytic activity by changing the dynamics of electron–hole recombination and inter facial transfer. More recently, H.W. Kang et al. reported $NaTaO_3$-C composite powder as efficient photocatalyst for the evolution of hydrogen from water splitting without adding any co-catalyst [20]. Therefore, detailed studies on coupled $NaTaO_3$ and their photocatalytic activities are important in order to develop $NaTaO_3$ based photocatalysts for solar energy application.

It is well known that catalytic behaviour is not only material dependent, but also size dependent. The one generalized behaviour of the materials is "Smaller the particle size, larger the specific

* Corresponding author. Tel.: +91 870 2462675; fax: +91 870 2459547.
E-mail addresses: vishnu@nitw.ac.in, santhu.chem@gmail.com (V. Shanker).

0025-5408/$ – see front matter © 2013 Elsevier Ltd. All rights reserved.
http://dx.doi.org/10.1016/j.materresbull.2013.09.013

surface area''. Therefore, the great demand of fine particles of this pervoskite oxide has stimulated a lot of activity towards their synthesis by soft chemical methods. A number of methods have been reported for the preparation of $NaTaO_3$ [21–25]. The conventional technique for preparing $NaTaO_3$ powder is mainly based on the solid state reaction, which requires long time and higher temperature (typically 1000–1300 °C). Recently, many efforts have been made to synthesize $NaTaO_3$, for example, He and Zhu have successfully synthesized the perovskite-type $NaTaO_3$ powder with a cubic morphology, via the solvothermal method [26]. Nelson and Wagner have obtained $NaTaO_3$ nanorods from $TaCl_5$ by the alkalide reduction method [27]. More recently, our group reported the modified reverse micellar route to synthesize nanocrystalline $NaTaO_3$ with an average particle size of about 40 nm (much smaller than other methods such as solid state, hydrothermal and sol–gel techniques) [28]. Reverse micellar route is one of the most successful techniques for preparing the nanosized metallic oxide materials with controlled geometric properties, such as surface morphology, surface area, and particle size. Reverse micellar route also avoids steps such as refluxing of alkoxides (sol–gel) result the uniform and homogeneous nanoparticles [29]. Moreover, the properties of composite catalyst are closely related to the fabrication processes such as sol–gel, hydrothermal and ultrasonic dispersion method. Especially, the ultrasonic dispersion technique is known to be a suitable route for synthesizing composite of two different semiconductor powders as it can easily control the solid solution with stoichiometric and homogeneous mixture. Since this method is a solution process, it allows flexibility to control the parameters with its relatively slow reaction process [30–33].

In this present work, first the nanocrystalline $NaTaO_3$ was prepared by modified reverse micellar method with average particle size of 43 nm and then g-C_3N_4/$NaTaO_3$ hybrid nanocomposites were prepared by a facile ultrasonic dispersion method at room temperature. The prepared samples were well characterized by PXRD, FTIR, TGA, FESEM, TEM and surface analyser. The photocatalytic activity of the prepared samples was evaluated for the degradation of Rhodamine B under both UV–visible and visible light irradiation. The recyclability of the as-prepared g-C_3N_4/$NaTaO_3$ hybrid nanocomposite was also investigated. However, to the best of our knowledge there is no report on the synthesis of g-C_3N_4/$NaTaO_3$ hybrid nanocomposite photocatalyst.

2. Experimental details

2.1. Materials

Melamine (Aldrich, 99.0%), tantalum isoprooxide (Aldrich, 10%, w/v; 99.9% metal based), tergitol NP9 (Aldrich, 99.0%), ethylene glycol (Qualigens, 99.5%), citric acid (Qualigens, 99.5%), cyclohexane (Qualigens, 99.5%), 1-octanol (Qualigens, 99.5%), sodium hydroxide (Merck, 98%) and Rhodamine B (Aldrich, 85.0%) were used as received. All other reagents used in this work were of analytically pure and used without further purification.

2.2. Method

The g-C_3N_4 was prepared by direct heating melamine to 550 °C for 2 h in N_2 atmosphere [34]. Nanocrystalline powder of $NaTaO_3$ has been synthesized by a modified reverse micellar method [28]. Preparation of g-C_3N_4/$NaTaO_3$ hybrid nanocomposites was as follows: In brief, an appropriate amount of g-C_3N_4 was ultrasonicated in 50 mL of methanol for 30 min. To this, 0.1 g of $NaTaO_3$ was added and stirred in a fume cupboard for 24 h. After evaporation of methanol, a solid product was obtained and dried at 100 °C for 1 h. The g-C_3N_4/$NaTaO_3$ photocatalysts with different weight ratios of g-C_3N_4, particularly 5% and 10% were synthesized and named as CNNTO5, and CNNTO10, respectively. The pure g-C_3N_4 named as CN and $NaTaO_3$ named as NTO.

2.3. Characterization

X-ray diffraction studies (XRD) were carried out on a Bruker D_8 Advance Diffractometer using Cu K_α radiation with Ni filter for striping Cu K_β radiation. TGA/DTA experiments were carried out on PerkinElmer Pyris Diamond TGA/DTA system on well ground samples in flowing nitrogen atmosphere with a heating rate 10 °C/min. The FTIR spectra were recorded in transmission mode from 4000 to 400 cm^{-1} on a Nicolate Protégé 460 FTIR spectrometer using KBr discs. FESEM studies of samples were carried out on a FEI quanta 3D FEG-FESEM operated at 10 kV by coating the powder sample with gold. TEM was done on a JEOL, JSM-6700F instrument. UV–vis diffuse reflectance spectra were recorded on a Lambda/20 Instruments (UV–vis NIR spectrophotometer), equipped with an integrating sphere to record the diffuse reflectance spectra of the samples, and $BaSO_4$ was used as a reference. The nitrogen adsorption–desorption isotherms were recorded using Quanta Chrome NOVA 1200e.

2.4. Photocatalytic activity

Rhodamine B (RhB), a widely used dye, was chosen as a model pollutant. The photocatalytic activity of the prepared samples (0.125 g) was examined by monitoring the degradation of RhB aqueous solution (250 mL, 5 mg L^{-1}) in a beaker under stirring condition at 250 rpm throughout the test at room temperature under both UV–visible and visible light irradiation. The visible light source for the photo-irradiation is solar simulator 300 W Xe lamp (Asahi Spectra Co., Ltd.) with a super cold filter, which provides the visible light region ranging from 400 nm to 700 nm and the light intensity is around 115 mW cm^{-2} and UV–visible light source for photo-irradiation is Hg lamp (125 W, Philips Co, Ltd). Prior to irradiation, solutions suspended with photocatalysts were stirred in dark condition for 30 min to ensure that surface of catalyst was saturated with RhB. During photocatalytic processes, the sample was periodically withdrawn, centrifuged to separate the photocatalyst powder from the solution, and used for the absorbance measurement. The absorption spectra were recorded on a UV–vis spectrophotometer. The photocatalytic activity of the hybrid nanocomposites compared with the pure g-C_3N_4 and $NaTaO_3$ under the same experimental conditions.

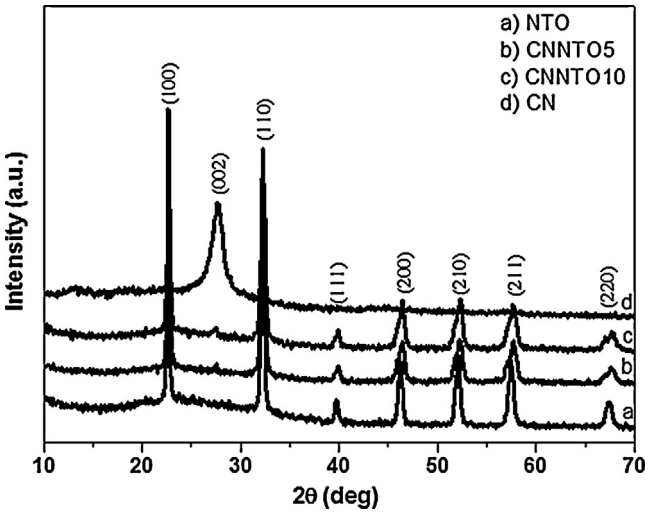

Fig. 1. XRD patterns of the prepared g-C_3N_4, $NaTaO_3$ and g-C_3N_4/$NaTaO_3$ photocatalysts.

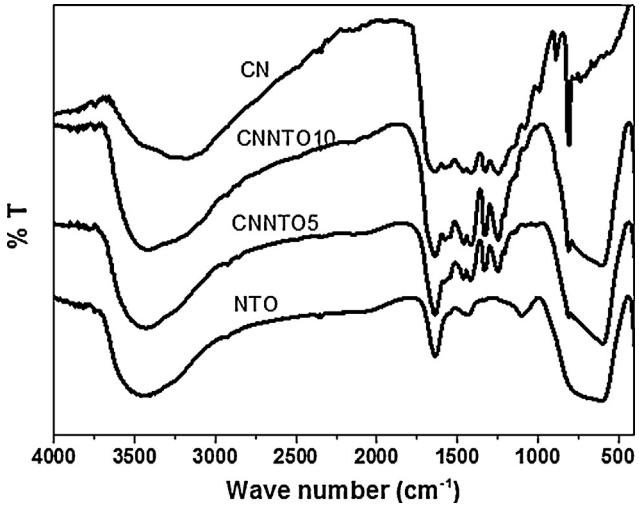

Fig. 2. FTIR of the prepared g-C_3N_4, $NaTaO_3$ and g-C_3N_4/$NaTaO_3$ photocatalysts.

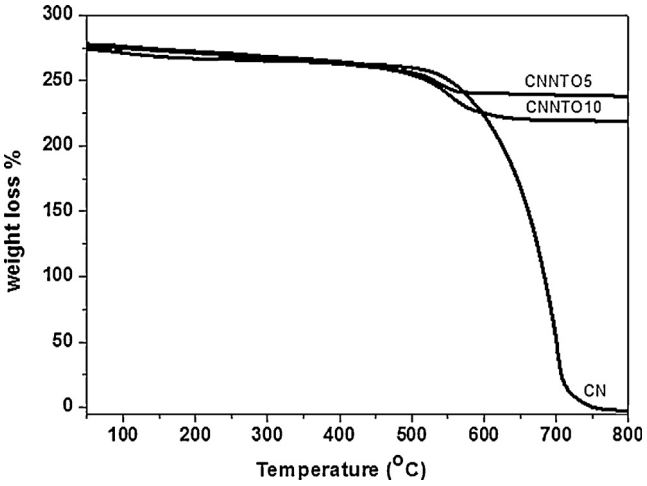

Fig. 3. TG curves of the prepared g-C_3N_4 and g-C_3N_4/$NaTaO_3$ photocatalysts.

3. Results and discussion

3.1. Characterization of photocatalysts

Fig. 1 shows the X-ray diffraction patterns of pure $NaTaO_3$, g-C_3N_4, and as-prepared g-C_3N_4/$NaTaO_3$ nanocomposite samples. Monophasic $NaTaO_3$ has been obtained by modified reverse micellar method followed by heat treatment at 600 °C for 12 h. All the reflections can be readily indexed as the cubic phase (JPCDS#742488). In the spectrum of hybrid nanocomposites, no change was observed in the crystal structure of $NaTaO_3$ but a new peak at 27.54 appears which is corresponding to the (0 0 2) plane of g-C_3N_4. A significant X-ray diffraction peak broadening in composite system indicates a decreasing crystallinity due to the loading with g-C_3N_4. However no impurity peak was found, indicating the presence g-C_3N_4 with $NaTaO_3$ to yield a novel two phase hybrid nanocomposite. The peak intensity of (0 0 2) plane was increased with increasing amount of g-C_3N_4 loading. The estimated average crystallite size of $NaTaO_3$ is 47.25 nm in pure $NaTaO_3$ and 46.13 nm in composite. The grain size was further supported by TEM results.

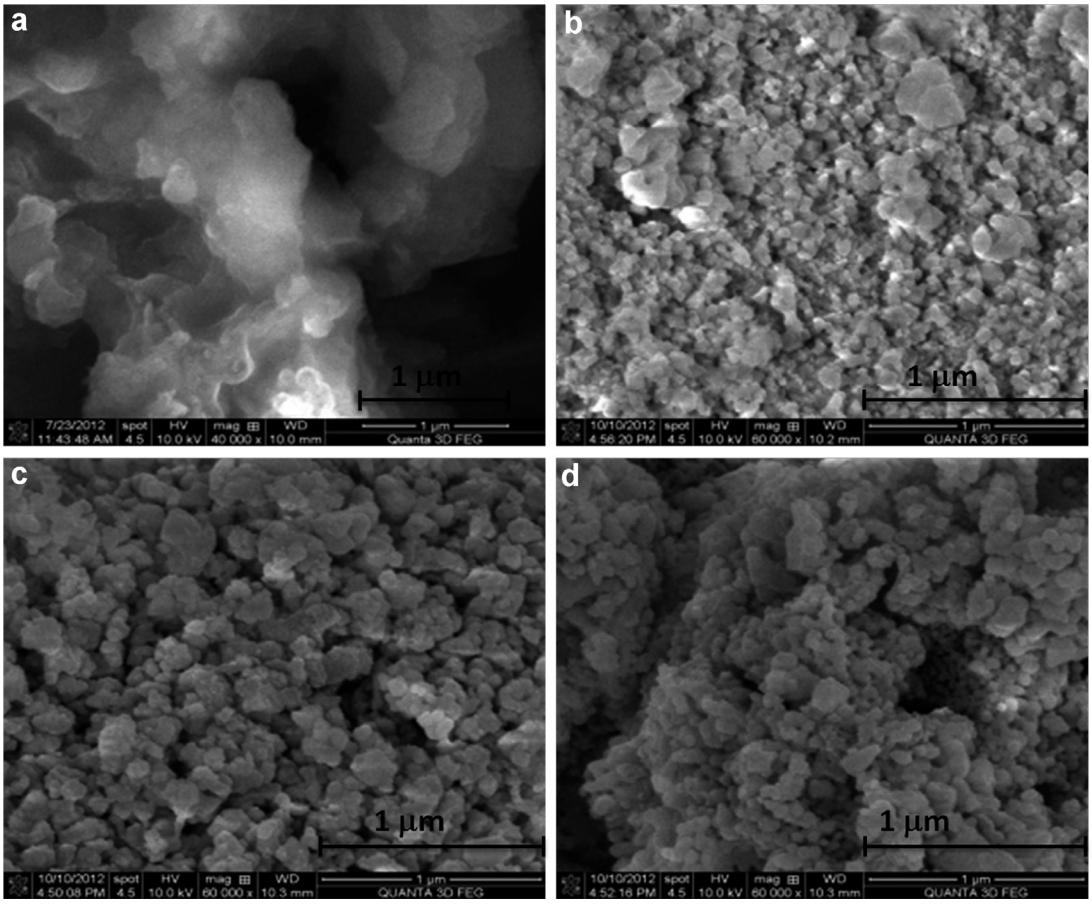

Fig. 4. FESEM of the prepared g-C_3N_4, $NaTaO_3$ and g-C_3N_4/$NaTaO_3$ photocatalysts: (a) pure $NaTaO_3$, (b) pure g-C_3N_4, (c) 5 wt% g-C_3N_4/$NaTaO_3$ and (d) 10 wt% g-C_3N_4/$NaTaO_3$.

Fig. 2 shows the FTIR spectrum of pure $NaTaO_3$, g-C_3N_4 and g-C_3N_4/$NaTaO_3$ hybrid nanocomposites. The broad Ta–O band in the powder sample heated above 500 °C is clearly visible in all compositions in the region 225–850 cm^{-1} [35]. However, a broad band was observed pertaining to adsorbed water around 3300–3600 cm^{-1} and 1658 cm^{-1} are corresponding to OH stretching vibrations, and another peak at 1384 cm^{-1} is corresponding to the H–O–H bending band of adsorbed H_2O molecules on the surface of sample. The IR-band due to adsorbed water arises as a result of water being released as a decomposition product and later gets adsorbed during the measurement. In the FTIR spectrum of g-C_3N_4, the broad band around 3100 cm^{-1} is indicating N–H stretching vibrations, the peaks at 1243 cm^{-1} and 1637 cm^{-1} were corresponding to the C–N and C=N stretching vibrations, respectively. The peak at 808 cm^{-1} was related to the s-triazine ring vibrations [36–38]. All characteristic peaks of g-C_3N_4 and $NaTaO_3$ were observed in g-C_3N_4/$NaTaO_3$ hybrid nanocomposite samples.

Thermogravimetric analysis of the dried sample of pure g-C_3N_4 and as-prepared hybrid nanocomposite samples performed as shown in Fig. 3. As can be seen that the decomposition of g-C_3N_4 starts at 550 °C and is completed at ~720 °C could be attributed to the burning of g-C_3N_4. This weight loss region could be seen in the g-C_3N_4/$NaTaO_3$ hybrid nanocomposite samples. The amount of g-C_3N_4 in the hybrid nanocomposite was calculated from the corresponding weight loss. The g-C_3N_4 in loaded 5, 10 weight percentages of g-C_3N_4/$NaTaO_3$ were found 4.94 wt% and 9.87 wt%, respectively. Therefore, the amount of g-C_3N_4 was nearly consistent to the loaded composition of g-C_3N_4.

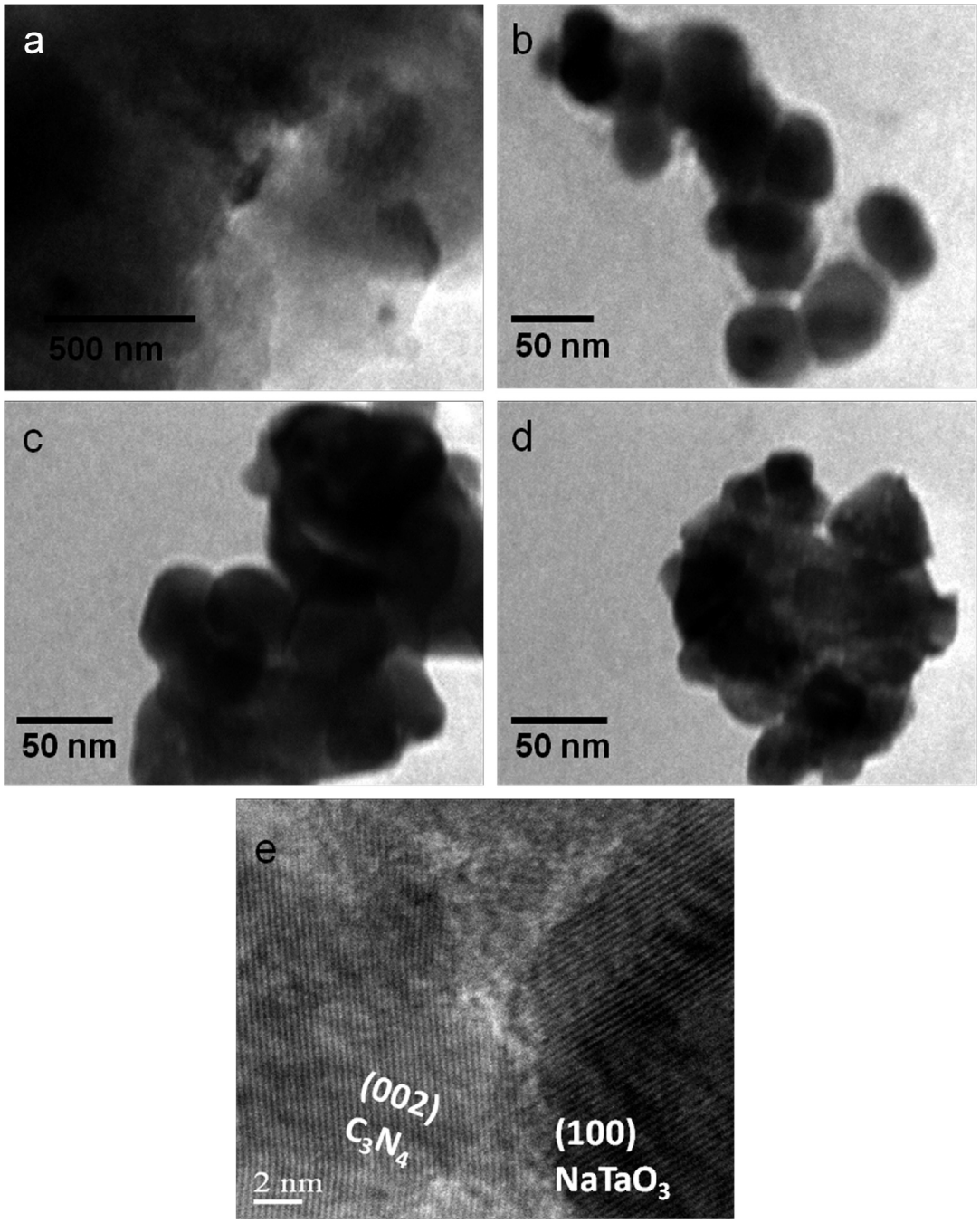

Fig. 5. TEM and HRTEM of the prepared pure g-C_3N_4, $NaTaO_3$ and g-C_3N_4/$NaTaO_3$ photocatalysts: (a) pure g-C_3N_4, (b) pure $NaTaO_3$, (c) 5 wt% g-C_3N_4/$NaTaO_3$, (d) 10 wt% g-C_3N_4/$NaTaO_3$ and (e) HRTEM of 5 wt% g-C_3N_4/$NaTaO_3$.

The morphology and nanostructures of the prepared samples were then investigated by FESEM and TEM. Fig. 4 shows the FESEM images of $NaTaO_3$ nanoparticles and g-C_3N_4/$NaTaO_3$ hybrid nanocomposites. It can be seen that the $NaTaO_3$ possesses cube morphology with high agglomeration. However, FESEM images have no enough resolution for the analysis of heterostructure and particle size distributions. TEM images (Fig. 5a) indicated that the average particle size of the prepared $NaTaO_3$ is 43 nm. Fig. 5b shows sheet structure of pure g-C_3N_4. The g-C_3N_4/$NaTaO_3$ nanocomposite showed almost similar morphology (Fig. 5c and d) as compared with $NaTaO_3$ nanoparticles. HRTEM studies confirm the formation of the interface between g-C_3N_4 and $NaTaO_3$ in the composite system (Fig. 5e). However, g-C_3N_4/$NaTaO_3$ hybrid nanocomposites also exhibit a certain degree of particle agglomeration.

Fig. 6 shows the UV–vis diffuse reflection spectra of pure $NaTaO_3$, g-C_3N_4 and as-prepared g-C_3N_4/$NaTaO_3$ hybrid nanocomposite samples. The pure $NaTaO_3$ and g-C_3N_4 samples show high photo-absorption in UV region around 314 nm and in visible region around 452 nm, consistent with white and light yellow colours, respectively. The g-C_3N_4/$NaTaO_3$ hybrid nanocomposite samples present photo-absorption in UV region around 320 nm as well as visible region around 460 nm, consistent with the pale yellow colour, suggesting that the composite catalysts have potential for the degradation of organic pollutants under visible light irradiation. The wavelength threshold is determined by elongating the baseline and steepest tangent of the UV–vis spectrum [39]. According to Kubelkae Munk function, the band gap energies of pure $NaTaO_3$ and g-C_3N_4 estimated to be 3.95 eV and 2.74 eV, respectively [40]. However, these above band gap energies were observed in composite system. These are 3.92 eV and 2.71 eV in CNNTO5, and 3.87 eV and 2.69 eV in CNNTO10, respectively. A slight red shift in the band edge positions of $NaTaO_3$ and g-C_3N_4 may be due to hybridization with g-C_3N_4 which can act as a sensitizer, suggesting that the recombination rate of photoinduced electron–hole pair successfully suppressed in the g-C_3N_4/$NaTaO_3$ hybrid nanocomposites.

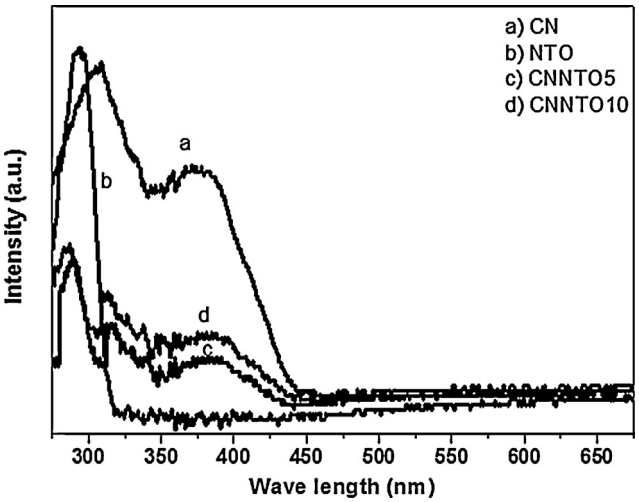

Fig. 6. UV–vis DRS of the prepared g-C_3N_4, $NaTaO_3$, and g-C_3N_4/$NaTaO_3$ photocatalysts.

Fig. 7 shows nitrogen adsorption–desorption isotherms of pure g-C_3N_4, $NaTaO_3$ and as-prepared g-C_3N_4/$NaTaO_3$ samples. The specific surface area of the NTO, CN, CNNTO5, and CNNTO10 was

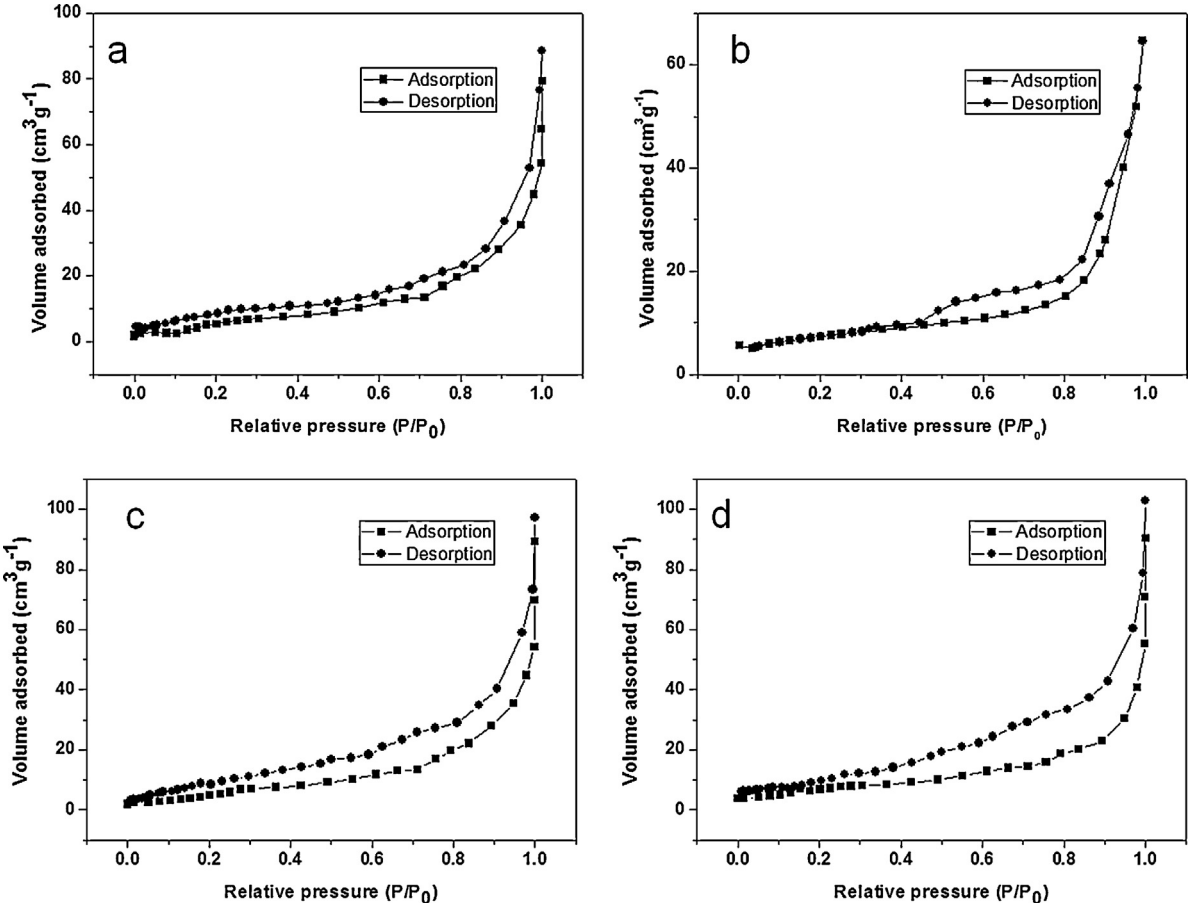

Fig. 7. Nitrogen adsorption–desorption isotherm of the prepared photocatalysts: (a) pure $NaTaO_3$, (b) pure g-C_3N_4, (c) 5 wt% g-C_3N_4/$NaTaO_3$ and (d) 10 wt% g-C_3N_4/$NaTaO_3$.

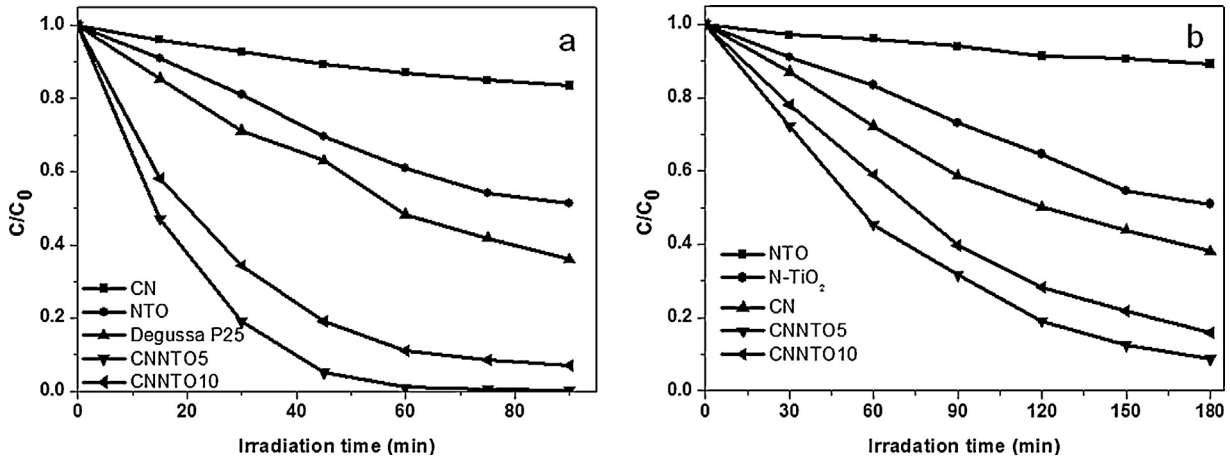

Fig. 8. (a) Comparison of photocatalytic activities of pure $NaTaO_3$, g-C_3N_4, Degussa P25 or N-doped TiO_2 and g-C_3N_4/$NaTaO_3$ for the degradation of RhB: (a) UV–visible light and (b) visible light irradiation.

found to be 22.18 $m^2 g^{-1}$, 8.13 $m^2 g^{-1}$, 23.26 $m^2 g^{-1}$ and 24.38 $m^2 g^{-1}$, respectively. Relatively, large specific surface area of the hybrid nanocomposite is useful for the better adsorption of organic compounds and also provides more number of reactive sites for photocatalytic process, thereby enhances the photocatalytic activity.

3.2. Photocatalytic activity

Fig. 8 shows the photocatalytic degradation of RhB with different photocatalyst under both UV–visible and visible light irradiation. The as-prepared g-C_3N_4/$NaTaO_3$ hybrid nanocomposites exhibits significantly enhanced photocatalytic activity compared to pure $NaTaO_3$, g-C_3N_4 and Degussa P25 (commercial TiO_2) under UV–visible light irradiation as shown in Fig. 8a. The dramatic photocatalytic activity is generated under visible light irradiation is due to the loading of g-C_3N_4 in which electron excited from VB to CB could directly inject into the CB of $NaTaO_3$, making g-C_3N_4/$NaTaO_3$ visible light driven photocatalyst. The visible light photocatalytic activity of CNNTO5 is much higher than that of pure g-C_3N_4 as well as commercial N-TiO_2. However, pure $NaTaO_3$ did not show the activity under visible light irradiation. The highest photocatalytic activity was obtained for CNNTO5 under both UV–visible and visible light irradiation. The blank test demonstrates that the irradiation without photocatalyst has little effect on the degradation process, suggesting the excellent photocatalytic activity of the hybrid nanocomposites under both UV–visible and visible light irradiation. The enhanced photocatalytic activity may be due to enhanced charge separation efficiency in the g-C_3N_4/$NaTaO_3$ system.

3.3. Reusability

The reusability of a photocatalyst can be considered as one of the important factors for practical applications. Interestingly, the g-C_3N_4/$NaTaO_3$ photocatalysts can be easily reused by simple filtration or low-speed centrifugation and thus avoids the second pollution. To study the reusability of the 5 wt% g-C_3N_4/$NaTaO_3$ photocatalyst, five successive photocatalytic experimental runs were carried out by adding used photocatalyst to fresh RhB solutions with no change in overall concentration of the catalyst under both UV–visible and visible light irradiation. The photocatalytic activity of 5 wt% g-C_3N_4/$NaTaO_3$ hybrid nanocomposite photocatalyst is retaining over 90% of its original activity after five successive experimental runs in both UV–visible and visible light irradiation as shown in Fig. 9. The XRD studies were performed for reused g-C_3N_4/$NaTaO_3$ photocatalyst (after five successive experimental runs) and no change was observed in the resulting spectrum which indicates the high structural stability of g-C_3N_4/$NaTaO_3$ (Fig. 10). Therefore, g-C_3N_4/$NaTaO_3$ nanocomposites can be used as high-performance visible light photocatalysts for environmental applications.

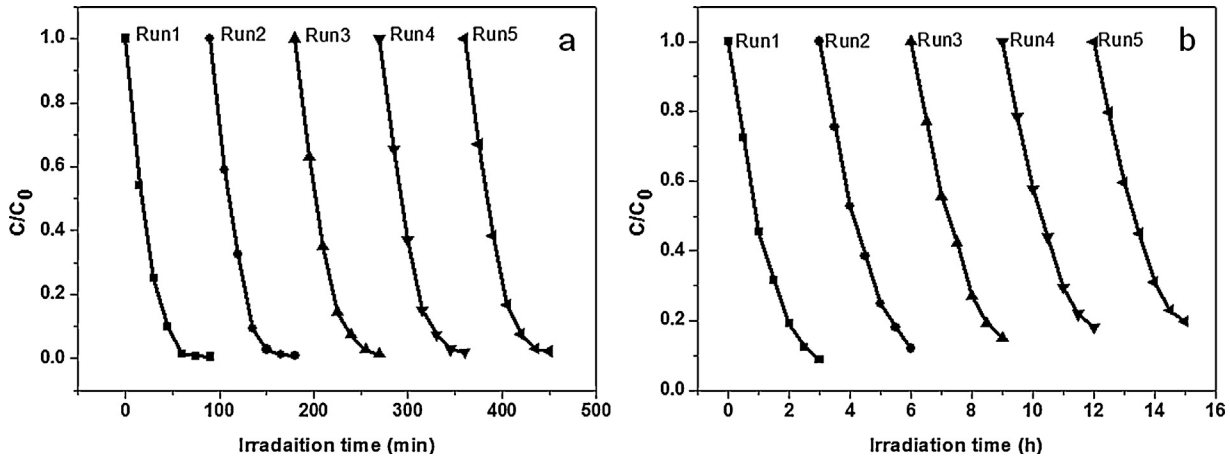

Fig. 9. Recyclability of CNNTO5 photocatalyst (five successive experiments) for the degradation of RhB: (a) UV–visible light and (b) visible light irradiation.

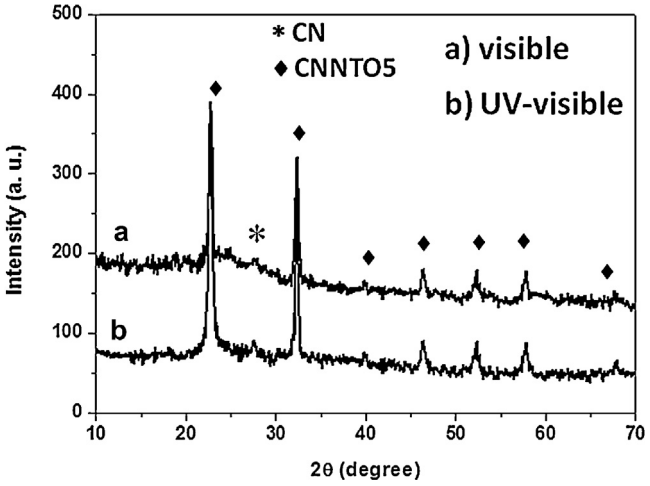

Fig. 10. The XRD pattern of the reused CNNTO5 sample after five successive experimental runs.

3.4. Mechanism for the enhanced photocatalytic activity of g-C_3N_4/$NaTaO_3$ hybrid nanocomposite

It is well known that phase structure, adsorption, and efficient charge separation of photoinduced charge carrier can play an important role for the enhancement of photocatalytic performance under light irradiation [41–44]. Our results clearly show that the crystal phase structure of $NaTaO_3$ was not changed after the hybridization with g-C_3N_4. The adsorption ability of the $NaTaO_3$ and g-C_3N_4/$NaTaO_3$ photocatalysts was also investigated in the dark condition for 30 min duration. The adsorption ability of g-C_3N_4/$NaTaO_3$ photocatalyst significantly higher than that of pure $NaTaO_3$ photocatalyst, indicating the adsorption of RhB in composite system is not simple physical adsorption but it is also contributed from π–π stacking between RhB and g-C_3N_4 which similar to the conjugation between aromatic molecules and graphene [45]. The enhanced adsorption ability was attributed for higher photocatalytic activity of the g-C_3N_4/$NaTaO_3$ hybrid nanocomposite system.

It is important to find out the role of reactive species, to propose a pathway for photocatalytic reaction. The role of reactive species in the photocatalytic reaction can be studied by the radicals and holes trapping experiments. However, methanol and ammonium oxalate (AO) can be used as radicals' scavenger and holes scavenger, respectively. As shown in Fig. 11a, a small change in the photocatalytic activity of the as-prepared CNNTO5 was observed under UV–visible light irradiation by addition of methanol of as •OH scavenger, whereas the photocatalytic activity was greatly suppressed by addition of AO as holes scavenge, indicating the photoinduced holes were primary reactive species in the g-C_3N_4/$NaTaO_3$ hybrid nanocomposite system under UV–visible light irradiation. On the contrary, the photocatalytic activity was highly suppressed by the addition of methanol as shown in Fig. 11b. However a small change in the activity was also observed by the addition of AO. These results clearly indicate that photoinduced radicals were primary reactive species in g-C_3N_4/$NaTaO_3$ hybrid nanocomposite system under visible light irradiation.

On the basis of our experimental results, a proposed mechanism is discussed to explain the enhanced photocatalytic activity of the as-prepared g-C_3N_4/$NaTaO_3$ nanocomposites for the degradation of RhB under both UV–visible and visible light irradiation. This is due to synergistic effects at interface of the $NaTaO_3$/g-C_3N_4. First, the high charge separation efficiency may be due to the energy level match between g-C_3N_4 and $NaTaO_3$. According to the previous reports, the redox potential of both conduction band (E_{CB} = −1.3 eV vs. NHE) and valence band (E_{VB} = +1.4 eV vs. NHE) of g-C_3N_4 are more negative than those of conduction band (E_{CB} = −0.98 eV vs. NHE) and valence band (E_{VB} = +2.96 eV vs. NHE) of $NaTaO_3$ [34,46]. A scheme for the separation and transport of photoinduced charge carrier at the interface of the g-C_3N_4/$NaTaO_3$ under UV–visible and visible light is shown in Figs. 12 and 13, respectively. As the g-C_3N_4/$NaTaO_3$ photocatalyst is irradiated with UV–visible light, the photoinduced holes migrates from $NaTaO_3$ to the valence band (VB) of g-C_3N_4, suppressing the electron–hole pair recombination. The photoinduced holes on $NaTaO_3$ could oxidize polluted dyes effectively. The photoinduced electrons in conduction band of $NaTaO_3$ can also migrate to the conduction band of g-C_3N_4 thereby reaches the surface of g-C_3N_4/$NaTaO_3$ hybrid nanocomposite photocatalyst where the electrons could reduce adsorbed surface O_2 to form various reactive oxygen species, thus could assist the degradation of organic pollutants. As a result, the enhanced photocatalytic activity is observed over g-C_3N_4/$NaTaO_3$ hybrid nanocomposite under UV–visible light irradiation by suppressing the charge recombination. Under visible light irradiation, a high-energy photon excites an electron from the VB to CB of g-C_3N_4. The photoinduced electrons in g-C_3N_4 could directly inject into the CB of $NaTaO_3$, reaches the catalyst surface where the electrons could reduced adsorb surface O_2 to various reactive species, thus could greatly enhance activity. Meanwhile, holes can transfer to the VB of g-C_3N_4 conveniently and assist in the

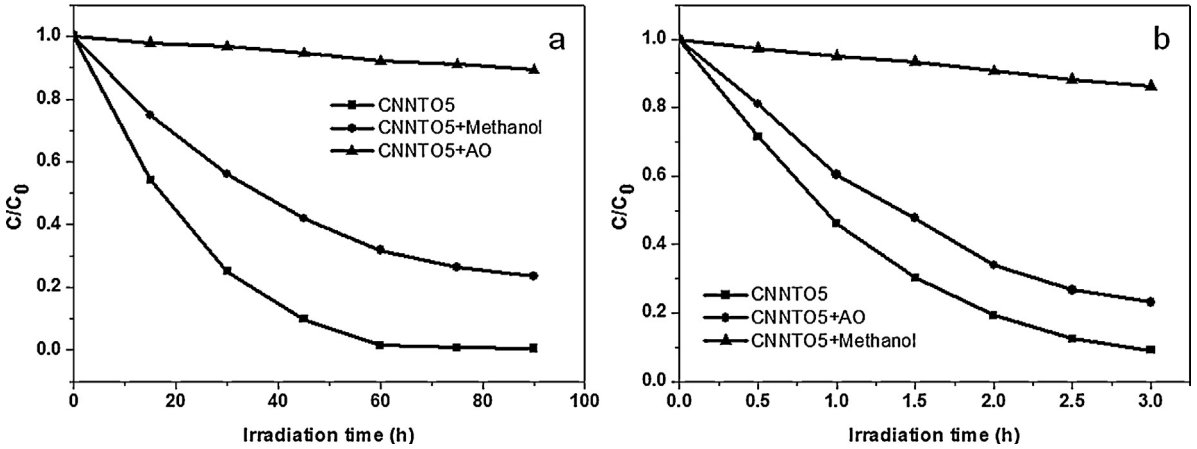

Fig. 11. The plots of photogenerated carriers trapping in the system of photodegradation of RhB by $NaTaO_3$ and g-C_3N_4/$NaTaO_3$: (a) UV–visible light and (b) visible light irradiation.

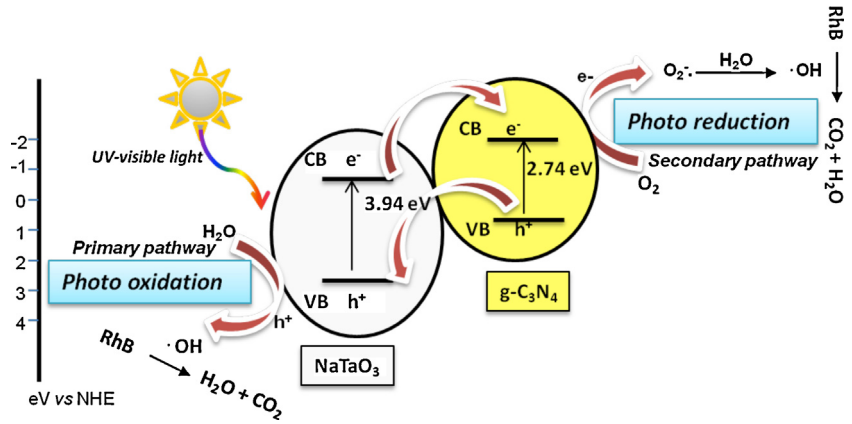

Fig. 12. Schematic drawing illustrating the mechanism of charge separation and photocatalytic activity of the g-C_3N_4/$NaTaO_3$ photocatalyst under UV–visible light irradiation.

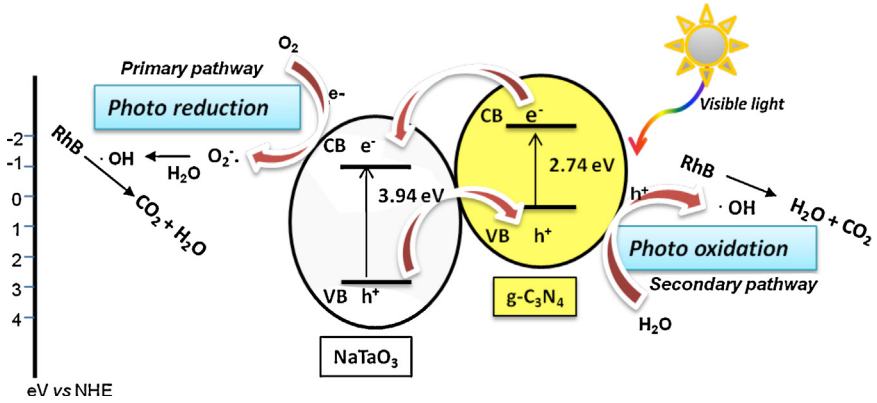

Fig. 13. Schematic drawing illustrating the mechanism of charge separation and photocatalytic activity of the g-C_3N_4/$NaTaO_3$ photocatalyst under visible light irradiation.

degradation of organic pollutant. As a result, the photogenerated electrons in g-C_3N_4 could directly inject into the CB of $NaTaO_3$, making g-C_3N_4/$NaTaO_3$ visible light driven photocatalyst. Hence dramatic photocatalytic activity is generated over g-C_3N_4/$NaTaO_3$ hybrid nanocomposite under visible light irradiation. Therefore, g-C_3N_4 can act as both electron acceptor and donor. Interestingly, the efficient electron migration from $NaTaO_3$ to g-C_3N_4 also promotes structural stability of the g-C_3N_4/$NaTaO_3$ photocatalyst by keeping electrons away from $NaTaO_3$. This effective charge separation by band potentials between two semiconductors is also reported in other systems, such as g-C_3N_4/TaON [47]. The g-C_3N_4 can act as an electron reservoir to trap electrons emitted from $NaTaO_3$ particles due to irradiation by UV–visible light, thus protecting the electron–hole pair from recombination probability in the g-C_3N_4/$NaTaO_3$ hybrid nanocomposite. These above aspects together attributed for the enhanced photocatalytic activity and improved stability of the novel g-C_3N_4/$NaTaO_3$ photocatalyst.

4. Conclusion

In summary, we have successfully prepared novel g-C_3N_4/$NaTaO_3$ nanocomposites by a facile ultrasonic dispersion method. Our results clearly show that the crystal structure and morphology of $NaTaO_3$ are not changed during the hybridization. Interestingly, the hybrid nanocomposites exhibited significantly enhanced photocatalytic activity for the degradation of RhB under both UV–visible and visible light irradiation. The highest efficiency was observed for 5 wt% g-C_3N_4/$NaTaO_3$ hybrid nanocomposite. The high photocatalytic performance could be attributed to synergistic effects which promote the migration efficiency of photoinduced electron–hole pair at the interface of the $NaTaO_3$/g-C_3N_4. More importantly, the as-prepared nanocomposite possesses high reusability. Therefore, it can be used as a promising photocatalyst for practical applications in environmental purification and clean hydrogen energy production from water splitting.

Acknowledgements

Authors thank DST, Government of India for financial support (SR/FT/CS-096/2009) and SAIF, AIIMS New Delhi for TEM facility. Santosh Kumar also thank MHRD, Government of India for a fellowship. The corresponding author also thank to Prof. A.K. Ganguli, Indian Institute of Technology Delhi, for carrying out part of this work in his lab.

References

[1] G. Suyal, E. Colla, R. Gysel, M. Cantoni, N. Setter, Nano Lett. 4 (2004) 1339.
[2] H. Kato, A. Kudo, Chem. Phys. Lett. 295 (1998) 487.
[3] A. Kudo, H. Kato, Chem. Phys. Lett. 331 (2000) 373.
[4] A. Kudo, H. Kato, I. Jsuji, Chem. Lett. 33 (2004) 1534.
[5] H. Kato, A. Kudo, J. Phys. Chem. B 105 (2001) 4285.
[6] C.C. Hu, C.C. Tsai, H. Teng, J. Am. Ceram. Soc. 92 (2009) 460.
[7] A. Yamakata, T. Ishibashi, H. Kato, A. Kudo, H. Onishi, J. Phys. Chem. B 107 (2003) 14383.
[8] A. Iwase, H. Kato, A. Kudo, ChemSusChem 2 (2009) 873.
[9] S.C. Yan, Z.Q. Wang, Z.S. Li, Z.G. Zou, Solid State Ionics 180 (2009) 1539.
[10] H. Kato, K. Asakura, A. Kudo, J. Am. Chem. Soc. 125 (2003) 3082.
[11] D.R. Liu, C.D. Wei, B. Xue, X.G. Zhang, Y.S. Jiang, J. Hazard. Mater. 182 (2010) 50.
[12] H. Fu, S. Zhang, L. Zhang, Y. Zhu, Mater. Res. Bull. 43 (2008) 864.
[13] Z.G. Yi, J.H. Ye, Appl. Phys. Lett. 91 (2007) 254108.

[14] I. Pastoriza-Santos, D.S. Koktysh, A.A. Mamedov, M. Giersig, N.A. Kotov, L.M. Liz-Marzán, Langmuir 16 (2000) 2731.
[15] L.W. Zhang, H.Y. Cheng, R.L. Zong, Y.F. Zhu, J. Phys. Chem. C 113 (2009) 2368.
[16] P. Wang, B. Huang, X. Qin, X. Zhang, Y. Dai, J. Wei, M.H. Whangbo, Angew. Chem. Int. Ed. 47 (2008) 7931.
[17] M. Li, X.F. Yu, S. Liang, X.N. Peng, Z.J. Yang, Y.L. Wang, Q.Q. Wang, Adv. Funct. Mater. 21 (2011) 1788.
[18] R. Wang, D. Xu, J.B. Liu, K.W. Li, H. Wang, Chem. Eng. J. 168 (2011) 455.
[19] P. Kanhere, J. Nisar, Y. Tang, B. Pathak, R. Ahuja, J. Zheng, Z. Chen, J. Phys. Chem. C 116 (2012) 22767.
[20] H.W. Kang, S.B. Park, Adv. Pow. Tech. 21 (2010) 106.
[21] I.C.M.S. Santos, L.H. Loureiro, M.F.P. Silva Ana, M.V. Cavaleiro, Polyhedron 21 (2002) 2009.
[22] G.K.L. Goh, F.F. Lange, S.M. Haile, C.G. Levi, J. Mater. Res. 18 (2003) 338.
[23] S. Wohlrab, M. Weiss, H. Du, S. Kaskel, Chem. Mater. 18 (2006) 4227.
[24] Y. He, Y. Zhu, N. Wu, J Solid State Chem. 177 (2004) 3868.
[25] X. Li, J. Zang, Catal. Commun. 12 (2011) 1380.
[26] Y. He, Y. Zhu, Chem. Lett. 33 (2004) 900.
[27] J.A. Nelson, M.J. Wagner, J. Am. Chem. Soc. 125 (2003) 332.
[28] V. Shanker, S.L. Samal, G.K. Pradhan, C. Narayana, A.K. Ganguli, Solid State Sci. 11 (2009) 562.
[29] A.K. Ganguli, A. Ganguly, S. Vaidya, Chem. Soc. Rev 39 (2010) 474.
[30] J.H. Bang, K.S. Suslick, Adv. Mater 22 (2010) 1039.
[31] X.-Y. Zhang, H.-P. Li, X.-L. Cui, Y. Lin, J. Mater. Chem. 20 (2010) 2801.
[32] W. Yao, B. Zhang, C. Huang, C. Ma, X. Song, Q. Xu, J. Mater. Chem. 22 (2012) 4050.
[33] C. Pan, J. Xu, Y. Wang, D. Li, Y. Zhu, Adv. Funct. Mater. 22 (2012) 1518.
[34] X. Wang, K. Maeda, A. Thomas, K. Takanabe, G. Xin, J.M. Carlsson, K. Domen, M. Antonietti, Nat. Mater. 8 (2009) 76.
[35] X. Li, J. Zang, J. Phys. Chem. C 113 (2009) 19411.
[36] M.J. Bojdys, J.O. Muller, M. Antonietti, A. Thomas, Chem. Eur. J. 14 (2008) 8177.
[37] Y. Zhao, D. Yu, H. Zhou, Y. Tian, O. Yanagisawa, J. Mater. Sci. 40 (2005) 2645.
[38] X. Li, J. Zhang, L. Shen, Y. Ma, W. Lei, Q. Cui, G. Zou, Appl. Phys. A: Mater. Sci. Process. 94 (2009) 387.
[39] W.H. Lin, C. Cheng, C.C. Hu, H. Teng, J. Appl. Phys. Lett. 89 (2006) 211904.
[40] Y. Lee, T. Watanabe, T. Takata, M. Hara, M. Yoshimura, K. Domen, Bull. Chem. Soc. Jpn. 80 (2007) 423.
[41] C. Pan, J. Xu, Y. Wang, D. Li, Y.F. Zhu, Adv. Funct. Mater. 22 (2012) 1518.
[42] S. Kumar, T. Surendar, A. Baruah, V. Shanker, J. Mater. Chem. A 1 (2013) 5333.
[43] K. Takanabe, K. Kamata, X. Wang, M. Antonietti, J. Kubota, K. Domen, Phys. Chem. Chem. Phys. 12 (2010) 13020.
[44] X. Zhou, B. Jin, R. Chen, F. Peng, Y. Fang, Mater. Res. Bull. 48 (2013) 1447.
[45] L.W. Zhang, H.B. Fu, Y.F. Zhu, Adv. Funct. Mater. 18 (2008) 2180.
[46] J.W. Liu, G. Chen, Z.H. Li, Z.G. Zhang, Int. J. Hydrogen Energy 32 (2007) 2269.
[47] S.C. Yan, S.B. Lv, Z.S. Li, Z.G. Zou, Dalton Trans. 39 (2010) 1488.